Modeling Multipath Effects on Frequency Locked Loops

Liangchun Xu, *Tufts University*
Jason Rife, *Tufts University*

ABSTRACT

This paper investigates the impact of non-line-of-site (NLOS) and multipath signals on frequency-locked loops (FLLs), which are commonly used to obtain Doppler shift measurements for velocity estimation in radio navigation. First, we use theory to model the effects of NLOS signals on the Doppler estimate produced by a conventional FLL with an arctangent discriminator. Next, we use experiments to verify theoretical predictions. A salient result is that, in the absence of a direct signal, a single NLOS signal does not corrupt Doppler observables if the angle-of-arrival (AOA) is known. Another striking result is that, in a multipath environment involving two signals, the arctangent discriminator (averaged over the beat frequency) tracks only the higher amplitude signal. Our investigation has particular significance for radio navigation in urban environments, either using global navigation satellite system (GNSS) signals or ground-based cellular signals.

INTRODUCTION

Non-line-of-site (NLOS) and multipath signals are common nuisances for wireless communication and positioning systems [1, 2]. NLOS signals arrive at the receiver on their own, while multipath refers to two or more replicas of a signal arriving at a receiver, typically including the direct line-of-site (LOS) signal in addition to one or more delayed NLOS signals. From the perspective of geometry-based navigation, NLOS signals and multipath signals are usually considered detrimental to both the pseudorange and the Doppler measurements. As such, various fault detection and exclusion (FDE) methods have been developed to identify and discard NLOS and multipath signals [1, 2, 3].

Despite their maligned history, NLOS and multipath signals have increasingly been recognized as potentially useful signals of opportunity. For instance, in urban applications of the global navigation satellite system (GNSS), reflection and shadowing models have been introduced to enable exploitation of NLOS pseudorange measurements [4, 5]. The potential for exploiting such signals of opportunity is perhaps even greater with the pending introduction of space-division multiple access (SDMA) systems in cellular networks [6]. In the near future, multiple-input, multiple-output (MIMO) and full-dimension MIMO (FD MIMO) technologies will be massively applied in cellular networks to increase the channel capacity. In these systems, stationary base stations will steer the transmit beam precisely toward the azimuth and elevation of mobile user receivers [7, 8]. Mobile users are also equipped with MIMO antennae in order to boost gain toward base stations and null undesirable multipath.

Although the multipath effects on code tracking in delay-locked loops (DLLs), and on carrier phase tracking in phase-locked loops (PLLs) are well studied [9, 10], the multipath effects on carrier frequency tracking in frequency-locked loops (FLLs) is not fully understood. In this paper, we investigate the effects of multipath on FLLs, both theoretically and experimentally. We seek to identify the mechanisms that degrade FLL-derived Doppler observables under multipath conditions. A key result is that the Doppler measurement for an individual NLOS signal can be interpreted geometrically using only angle of arrival (AOA), without knowledge of reflector geometry, so long as reflectors are stationary. For multipath signals consisting of two components, the amplitude ratio between the two arriving signal components plays a pivotal role in FLL performance. Specifically, the FLL tracks the Doppler shift of the signal component with larger amplitude. This generalization is true at least to the extent that the loop filter suppresses periodic perturbations at the beat frequency, which results from the Doppler-shift difference between the two arriving signal components. This generalization is striking because it indicates the FLL essentially tracks only one component of two-ray multipath: either the LOS signal or an NLOS signal component, but not both.

Better understanding the impact of multipath on FLLs has several practical implications. Importantly, error models enable better characterization of the degradation of FLL-derived Doppler measurements, particularly in urban applications where multipath is strong [3]. In the longer term, a better understanding of multipath on Doppler observables might also help in exploiting NLOS signals as additional signals-of-opportunity to improve navigation performance. For example, leveraging the observation that Doppler measurements are not corrupted by a reflection from a stationary surface, we propose a system concept that could exploit NLOS measurements using a MIMO antenna.

Our investigation of multipath effects on FLLs is structured as follows. First, as background, we review a general model of multipath. Second, we use theory and numerical models to characterize the effect of multipath on an FLL. Third, we introduce experimental results to provide context for our theoretical models and to demonstrate the deleterious impact of multipath on the Doppler observable for a conventional receiver. Fourth, we propose a concept for a future MIMO receiver that would leverage NLOS Doppler observables to enhance velocity estimation. A brief discussion of future work and a summary conclude the paper.

BACKGROUND

This section reviews standard approaches for modeling multipath in radio-navigation applications. As a starting point, let us consider a case like that illustrated in Fig. 1, where a transmitted signal can take both a direct LOS path to the receiver and an indirect NLOS path. We assume, the NLOS signal reflects from a stationary surface.

Both signal pathways are generated from the same transmitted signal. The transmitted signal s_T consists of a pseudorandom code c modulated on a carrier wave that oscillates at a frequency ω:

$$s_T(t) = A_T e^{j(\omega t)} c(t) \tag{1}$$

Here A_T is the amplitude of the transmitted signal and t is time. The components of the compound signal that arrives at the user antenna are labeled s_l, where the index l is 0 for the LOS path and a positive integer for each NLOS path. Each path may have a distinct Doppler shift $\omega_{d,l}$. For instance, the direct signal component features a Doppler shift $\omega_{d,0}$, which depends on the relative motion between the receiver and the transmitter. Note that in the signal model we do not consider the navigation bits because we assume that the discriminator is not computed across bit transitions [10].

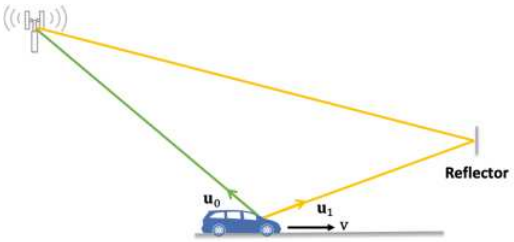

Fig. 1. Example of a multipath signal consisting of a direct LOS signal (green) superposed with an indirect NLOS signal (yellow). Outward unit vectors describe bearing from the receiver antenna to the source of the transmission in the case of the LOS signal ($\mathbf{u}_0$) or to the reflector in the case of the NLOS signal ($\mathbf{u_1}$).

A model for the LOS signal component s_0 may be written in the following form.

$$s_0(t) = A_0(t) e^{j\left((\omega+\omega_{d,0})t+\phi_0\right)} c(t-\tau_0) + n(t) \tag{2}$$

Here the initial carrier phase offset ϕ_0 and the code time delay τ_0 depend on time-of-flight and possibly other propagation effects, such as phase shifts due to reflection. The direct component is degraded by spreading losses, which determine its amplitude A_0, and by thermal noise, which is modeled as an additive random variable n.

The direct signal component combines with indirect NLOS signals arriving at the user antenna. In Fig. 1, there is only one NLOS signal, but in general there may be a number L of indirect signals that arrive at the user antenna. Modeling the NLOS components in a manner analogous to (2) and summing with the LOS signal gives the total received signal s:

$$s(t) = \sum_{l=0}^{L} \left(A_l(t) e^{j\left((\omega+\omega_{d,l})t+\phi_{0,l}\right)} c(t-\tau_l) \right) + n(t) \tag{3}$$

Note that the random noise variable n is modeled as a single term for the user receiver, and not as separate terms for each signal component. By analyzing (3), we can infer the effects of multipath on receiver observables, such as pseudorange and Doppler measurements, as a function of the parameters for each raypath ($A_l, \phi_{0,l}, \omega_{d,l}, \tau_l$).

In the following sections, we will analyze the effect of multipath on FLL-derived Doppler estimation for the two-ray case; first, as context, it is instructive to review existing models describing how multipath degrades the pseudorange observable.

Models of the impact of multipath on the pseudorange observable have been studied extensively for GPS applications [11], where the pseudorange observable is most typically obtained as the output of a DLL. Multipath distorts the correlation peak tracked by the DLL and, most typically, increases the apparent pseudorange as measured by the DLL (up to 1.5 code chips delay). Typical multipath error for code pseudorange is 1-5 m.

The code multipath effect can be visualized as a distortion of the ideal correlator peak for the direct signal, arriving at time τ_0 as described in (2), due to the arrival of NLOS signals, each delayed by a time τ_l as described in (3). This effect is shown below in Fig. 2, which plots correlator outputs as a function of time, measured in chips (where one chip corresponds to one bit of code). For a pseudocode that consists of a series of random digital bits, the individual autocorrelation functions are predominantly triangular in shape, as shown by the direct (dashed) and NLOS (solid) signals, which are considered individually on the left side of Fig. 2. When the LOS and NLOS signals are superposed, however, the combined correlator output is no longer triangular, as shown on the right side of Fig. 2, which shows the output of the correlator to the superposed LOS and NLOS signals, with the peak value normalized to one. The result is distorted, with an implied peak that is shifted later in time, nearly a full chip later in this case. When the peak location is extracted, for instance using an early-late discriminator as an input to a DLL [9], then the apparent time-of-flight is extended and the observed pseudorange is artificially increased.

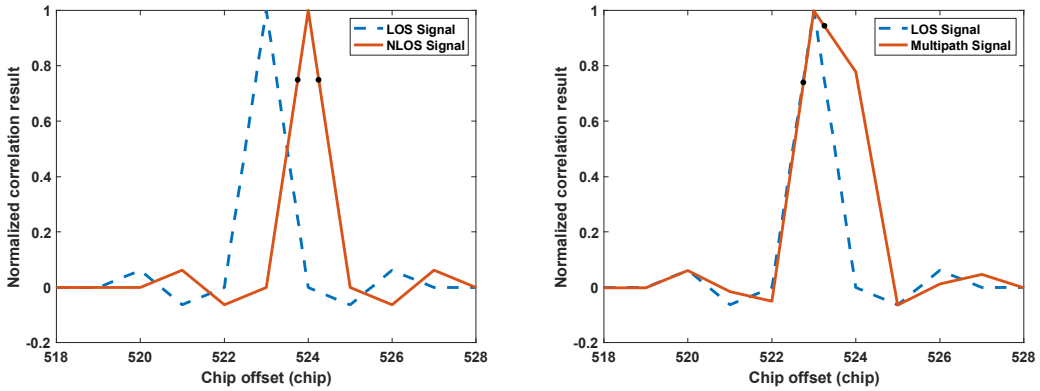

Fig. 2. Auto-correlation result of the NLOS signal (left) and the multipath signal (right)

The multipath effect on the PLL is also well studied [9]. By a two-ray analysis, the carrier-phase varying under multipath is no more than a quarter cycle (around 1-5 cm). However, the carrier phase measurement is fragile under severe multipath environment and it needs correct ambiguity fix, which is also challenging with multipath interference.

In contrast, the multipath effect on frequency tracking is not investigated yet.

For applications requiring reliable velocity estimation, the FLL-derived Doppler shift observable has several advantages over PLL and DLL-derived observables. The advantages are particularly salient for urban environments with strong multipath. First, an FLL is more resilient than a PLL in the face of structural occlusions that cause low carrier-to-noise ratio (C/N_0). In this environment, the FLL can tolerate larger tracking errors and, unlike the PLL, is not subject to cycle-slip induced errors. Second, Doppler observables are much less noisy than velocity estimates obtained by differencing DLL-derived pseudoranges, by an order of magnitude or more. In order to leverage these benefits, we introduce a mathematical model for multipath effects on FLLs in the following section.

MULTIPATH EFFECTS ON FREQUENCY LOCKED LOOPS

This section for the first time provides a theoretical characterization of how multipath affects the FLL output and its Doppler observable. Acknowledging that many approaches exist for implementing an FLL, in this work, we attempt to generalize the FLL somewhat, to capture a wide range of FLL implementations. Our generalized model consists of sequence of four signal processing steps labeled the coherent integration (also known as code and carrier wipeoff), discriminator, non-coherent moving average, and loop filter blocks. These blocks are shown in Fig. 3 The output of the loop filter block is used to update the estimated

Doppler frequency, which is in turn used to steer the numerically controlled oscillator (NCO) and adjust the code replica that is compared against the received signal as an input to coherent averaging.

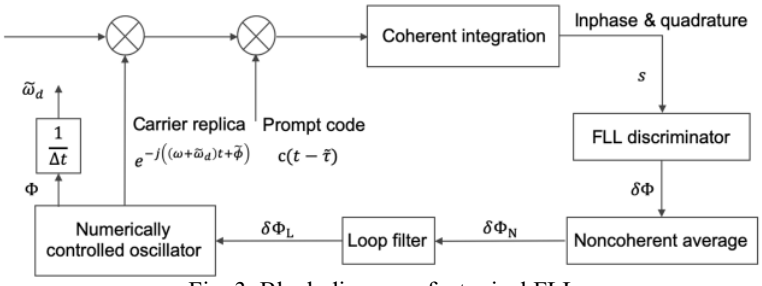

Fig. 3. Block diagram of a typical FLL

In our subsequent analysis, we will assume that the coherent integration block removes the code term $c(t)$ from the input signal. The coherent integration preserves the signal's phase [9], such that the real and imaginary parts (inphase and quadrature components) of (3) are available for processing by the discriminator block. As such, the subsequent sections will focus on analyzing the discriminator and, for multipath cases causing the discriminator output to vary quickly in time, also on the subsequent filtering blocks shown in the figure.

FLL Observable for LOS-only Signal

As a first step in modeling the FLL, this section considers the baseline case when the input signal consists only of an LOS component uncorrupted by multipath.

In our analysis we assume that the discriminator of Fig. 3 is an arctangent discriminator. Though the arctangent discriminator is more computationally complex than alternatives sometimes implement (e.g. than the cross-product discriminator described in [9]), we focus on the arctangent discriminator because of its ability to handle relatively large deviations in Doppler frequency between the signal samples.

The arctangent discriminator Φ is the phase of the received signal sample $s(t)$ and the complex conjugate of an earlier value $s'(t-\Delta t)$. In this section $s(t)$ is considered after the coherent integration as shown in Fig. 3.

$$\Phi = \angle s(t)s'(t-\Delta t) = \angle ss'_\Delta \tag{4}$$

Note that the subscript Δ will be used as a shorthand for the earlier timestamp. The prompt signal s is given by (3). The delayed signal is $s(t-\Delta t)$, where Δt is a small offset that is selected as an FLL design parameter. For instance, if Δt is set to the coherent integration time, then $s(t-\Delta t)$ is simply the adjacent output of the coherent integration block. The above phase-angle formula can be written equivalently as

$$\Phi = \text{atan2}\left(\frac{\text{Im}(ss'_\Delta)}{\text{Re}(ss'_\Delta)}\right) \tag{5}$$

In the absence of multipath, when only a single component is received, these two signals can be decomposed into deterministic phase and magnitude plus noise.

$$s = Be^{j\theta} + n \tag{6}$$
$$s_\Delta = B_\Delta e^{j\theta_\Delta} + n_\Delta \tag{7}$$

where the variables B and B_Δ describe the output amplitudes of the coherent integration block (shown in Fig. 3) and where

$$\theta = (\delta\omega_d)t + \phi_0 \tag{8}$$
$$\theta_\Delta = (\delta\omega_d)(t-\Delta t) + \phi_0 \tag{9}$$

Ideally, if tracking were perfect, the replica would match the arriving signal and so the coherent integration step would produce an output with zero Doppler error $\delta\omega_d$; in reality, the phase angles θ and θ_Δ are shifted by a small nonzero Doppler-estimation error, as described by (8) and (9). The time step Δt is assumed to be sufficiently short that the Doppler error $\delta\omega_d$ can be treated

as constant across the sequential samples s and s_Δ. In this paper, furthermore, we will neglect the contributions of noise, and focus on the deterministic outputs of the discriminator (noting that an analysis of noisy signals is an important topic for future work). The product ss'_Δ is thus

$$ss'_\Delta = BB_\Delta e^{j(\theta-\theta_\Delta)} \tag{10}$$

The coherent integration doesn't change the signal phase, as long as the two raypath frequencies are sufficiently close (e.g. when the receiver is moving at automotive speeds and slower). The arctan discriminator outputs the phase angle of the above equation:

$$\delta\Phi = \angle(ss'_\Delta) = \theta - \theta_\Delta = (\delta\omega_d)\Delta t \tag{11}$$

In the FLL loop, as shown in Fig. 3, each difference $\delta\Phi$ measured by the discriminator reflects the instantaneous Doppler error between the current and previous signals. These instantaneous errors are passed through the filtering blocks (labeled "noncoherent average" and "loop filter" in the graphic, with outputs $\delta\Phi_N$ and $\delta\Phi_L$ respectively), and accumulated at the NCO to estimate Doppler as Φ. Here the subscript N indicates smoothing due to noncoherent averaging and the subscript L indicates additional smoothing due to the loop filter.

Assuming linear filtering, the FLL-observable can be computed equivalently by switching the order of the filtering and accumulation operations. As such, we will define an accumulated discriminator variable Φ, which represents integration by the NCO if filtering were removed. That is

$$\Phi = \int \delta\Phi \mathrm{dt} = (\omega + \omega_d)\Delta t \tag{12}$$

Here the baseband frequency ω is a known offset that is included in initialization of the loop filter. Absent high-frequency changes in the Doppler frequency, the filtering blocks in Fig. 3 will not have any significant effect on the values $\delta\Phi$ (that is $\delta\Phi \approx \delta\Phi_N \approx \delta\Phi_L$), so the estimate provided by (12) is a good approximation of the estimate accumulated by the NCO. Manipulating (12) we obtain a Doppler frequency estimate as:

$$\widetilde{\omega}_d = \frac{\Phi}{\Delta t} - \omega \tag{13}$$

Here the tilde superscript implies an estimated quantity. The estimated Doppler frequency reflects the combined contributions of the receiver and transmitter motion. As a reasonable approximation, the Doppler contributions of the receiver and transmitter, ω_r and ω_t, sum to give a combined Doppler shift for the direct signal:

$$\omega_d \approx \omega_r + \omega_t \tag{14}$$

Combining (13) with (14), and assuming the transmitter motion contribution is well characterized, we can estimate the receiver contribution to the Doppler shift as $\widetilde{\omega}_r$:

$$\widetilde{\omega}_r = \frac{\Phi}{\Delta t} - \omega - \omega_t \tag{15}$$

The transmitter contribution ω_t is assumed to be well characterized in the sense that it can be computed from broadcast parameters (in the case of GNSS) or that it is zero (in the case of a stationary terrestrial base station). Note in this case we consider only large stationary reflectors, and so (14) does not need to be modified to account for reflector motion.

The receiver's Doppler contribution can be used to infer the user-receiver velocity. The receiver Doppler contribution ω_r is related to the projection of the receiver velocity $\mathbf{v_r}$ onto the LOS direction:

$$\omega_r = -\frac{2\pi}{\lambda}\mathbf{v_r}\cdot\hat{\mathbf{u}}_r = -\frac{2\pi\|\mathbf{v}_r\|}{\lambda}\cos(\theta_r) \tag{16}$$

Here the carrier wavelength is λ and unit pointing vector in the direction of the arriving signal is $\hat{\mathbf{u}}_r$. Two forms of the velocity relationship are presented; the second replaces the dot product with an arrival angle θ between the pointing vector and the velocity vector.

Period-Averaged FLL Observable for NLOS and Multipath Cases

The subsection extends the previous FLL discriminator to include cases other than the LOS-only case. Noting that the coherent integration process does not significantly distort the phase of the incoming signals, we simplify our analysis by directly constructing our model of the discriminator output from the equation for the received signal equation prior to coherent integration, as described (3).

When multiple signal components (LOS and NLOS) combine, our model for the discriminator input becomes:

$$s = \sum_{l=0}^{L} B_l e^{j\theta_l} + n \tag{17}$$

Here the subscript l is introduced to index different signal components from 0 to L, where 0 indicates the LOS signal. Each individual component has a different propagation path, implying a distinct unit vector $\hat{\mathbf{u}}_{r,l}$ and accordingly, from (16), a distinct value of receiver Doppler $\omega_{r,l}$. The distinct values of $\omega_{r,l}$ further imply, through (13), that each signal component features a distinct values of Doppler shift, labeled $\omega_{d,l}$. Leveraging this distinction, we can expand the angles in (17) as

$$\theta_l = (\omega + \omega_{d,l})t + \phi_{0,l} \tag{18}$$

Note that the same baseband frequency ω is assumed for all the signal components.

In order to evaluate multipath effects on the FLL, the next step is to consider how the input model (17) maps through the discriminator (5). This mapping determines whether there is a bias for FLL tracking.

The remainder of this section considers this discriminator mapping of multipath in three steps. First, we consider the simple case when there is only one NLOS signal and no LOS signal. Second, we consider the simple case for a stationary receiver. Third, we consider the case when a two-ray pair, consisting of the LOS signal and one NLOS signal, arrive at the receiver. These three analyses are organized into remarks, below. These remarks will provide a basis, later, for interpreting experimental data.

Remark 1: [NLOS-only case] When one NLOS signal arrives at a receiver after reflecting from a stationary surface and when the LOS signal is absent, the Doppler observable is proportional to receiver velocity projected on the NLOS path.

Discussion: As shown in Fig. 1, the NLOS signal arrives at the receiver along the raypath from the receiver to the location of the reflection. If the unit vector along the arriving raypath is labeled $\hat{\mathbf{u}}_{r,l}$ then (16) can be generalized to describe the projection of the vehicle velocity onto that raypath direction.

$$\omega_{r,l} = -\frac{2\pi}{\lambda}\mathbf{v_r} \cdot \hat{\mathbf{u}}_{r,l} = -\frac{2\pi\|\mathbf{v}_r\|}{\lambda}\cos(\theta_{r,l}) \tag{19}$$

Each raypath has a different Doppler shift $\omega_{r,l}$ due to receiver motion, because each raypath direction is distinct. Likewise, the angle $\theta_{r,l}$ between the unit vector and the velocity vector is distinct for each raypath.

If only one NLOS signal is received ($l = 1$) and no direct signal is received, then it is easy to substitute (19) for (16) in the analysis of the prior section. By extension, the FLL will estimate $\omega_{r,1}$ the Doppler frequency obtained by projecting the receiver velocity $\mathbf{v_r}$ on to the NLOS raypath unit vector $\hat{\mathbf{u}}_{r,1}$.

Remark 2: [Zero-speed multipath case] When the receiver and reflective surfaces are stationary, multipath signals have no effect on the Doppler observable.

Discussion: When the receiver is stationary, the receiver speed is $\|\mathbf{v}_r\| = 0$. The receiver-motion contribution to Doppler shift $\omega_{r,l}$ can be computed by (19) for all raypaths to be

$$\omega_{r,l} = 0 \tag{20}$$

In practice, the transmitter-motion contributions are equal for all raypaths. This would not be guaranteed in general, as the transmitter-motion contribution to Doppler depends on the pointing vector from the transmitter to the receiver (for the LOS

raypath) or on the pointing vector from the transmitter to the reflection point (for NLOS raypaths). However, all of these pointing vectors are equivalent if the transmitter is far enough away (as in satellite navigation). Alternatively, if the transmitters are stationary terrestrial antennae (as in the case of cellular navigation), then the pointing vectors are not identical for all raypaths, but the transmitter velocity is zero, so ω_t is also zero.

Thus, when the receiver and reflective surfaces are motionless, the total Doppler shift is $\omega_d \approx \omega_t$. This is again a trivial extension of the analysis in the prior section. When the Doppler shift is equal for all raypaths, the summation of signals in (17) becomes

$$s_k = \sum_{l=0}^{L} \left(B_{l,k} e^{j\left((\omega+\omega_d)t+\phi_{0,l}\right)} \right) \tag{21}$$

This is a summation of sine waves with the same frequency but different phase shifts. These waves interfere to give the following expression, which can be obtained by factoring the time-varying term from (21).

$$s = B_{sum} e^{j((\omega+\omega_d)t)} \tag{22}$$

$$B_{sum} = \sum_{l=0}^{L} B_{l,k}\, e^{j\phi_{0,l}} \tag{23}$$

The structure of (22) is identical to the structure of (6), which is to say both model a sinusoid at a single frequency. As such, the analysis of the prior section can be used to extract ω_d and infer that the receiver velocity is zero. The multipath in no way biases or distorts this analysis.

Remark 3: [Nonzero-speed multipath case]. When multipath arrives at a moving receiver via two raypaths and when reflective surfaces are stationary, the period-average of the arctan discriminator tracks the signal component with higher power.

Discussion: When the multipath signal consists of only two components arriving on different raypaths, then we model the discriminator input as

$$s = B_0 e^{j\theta_0} + B_1 e^{j\theta_1} \tag{24}$$

where $\theta_l = \left(\omega + \omega_{d,l}\right)t + \phi_{0,l}$. In order to analyze how the arctangent discriminator processes (24), it is useful to factor the signal by introducing two variables of substitution. The first describes a phase difference, and the second a phase average.

$$\gamma = \frac{\theta_0 - \theta_1}{2}, \qquad \mu = \frac{\theta_0 + \theta_1}{2} \tag{25}$$

Substituting these variables into (24) gives

$$s = e^{j\mu}(B_0 e^{j\gamma} + B_1 e^{-j\gamma}) \tag{26}$$

The product ss'_Δ becomes

$$ss'_\Delta = e^{j(\Delta\mu)}\left((B_0^2 + B_1^2)\cos(\Delta\gamma) + 2B_0B_1\cos(\delta) + j(B_0^2 - B_1^2)\sin(\Delta\gamma)\right) \tag{27}$$

The parameters in this expression are

$$\Delta\mu = \mu - \mu_\Delta \tag{28}$$

$$\Delta\gamma = \gamma - \gamma_\Delta \tag{29}$$

$$\delta = \gamma + \gamma_\Delta \tag{30}$$

These parameters can be expanded using (25) and (18) to show they are equivalent to

$$\Delta\mu = \left(\omega + \frac{\omega_{d,0} + \omega_{d,1}}{2}\right)\Delta t \tag{31}$$

$$\Delta\gamma = \frac{\omega_{d,0} - \omega_{d,1}}{2}\Delta t \tag{32}$$

$$\delta = (\omega_{d,0} - \omega_{d,1})t - \Delta\gamma + \phi_{0,0} - \phi_{0,1} \tag{33}$$

The product ss'_Δ can be written as follows to reveal its phase

$$ss'_\Delta = e^{j\left(\Delta\mu + \text{atan2}\left(\frac{(B_0^2 - B_1^2)\sin(\Delta\gamma)}{(B_0^2 + B_1^2)\cos(\Delta\gamma) + 2B_0B_1\cos(\delta)}\right)\right)} \tag{34}$$

The arctangent discriminator (5) extracts the phase angle of (34), so the accumulated discriminator output Φ can be written

$$\Phi = \Delta\mu + \text{atan2}\left(\frac{(B_0^2 - B_1^2)\sin(\Delta\gamma)}{(B_0^2 + B_1^2)\cos(\Delta\gamma) + 2B_0B_1\cos(\delta)}\right) \tag{35}$$

The only time-dependent term in (35) is $\cos(\delta)$. Noting that δ is a linear function of time, according to (33), we can conclude that the accumulated discriminator Φ is a periodic function of time with a period $T = \frac{2\pi}{|\omega_{d,0} - \omega_{d,1}|}$. Exploiting this periodicity, we can compute <Φ>, the period-averaged value of (35). Eliminating one additional parameter by introducing the amplitude ratio $\beta = B_1/B_0$, the average discriminator output over a full period of δ values (from 0 to 2π) is

$$\langle\Phi\rangle = \Delta\mu + \frac{1}{2\pi}\int_0^{2\pi} \text{atan2}\left(\frac{(1-\beta^2)\sin(\Delta\gamma)}{(1+\beta^2)\cos(\Delta\gamma) + 2\beta\cos(\delta)}\right)d\delta \tag{36}$$

We have not been able to integrate this quantity analytically; however, we have been able to use numerics to obtain a remarkable solution for $f(\beta, \Delta\gamma)$, a normalized version of the integral in (36). Define

$$f(\beta, \Delta\gamma) = \frac{1}{2\pi(\Delta\gamma)}\int_0^{2\pi} \text{atan2}\left(\frac{(1-\beta^2)\sin(\Delta\gamma)}{(1+\beta^2)\cos(\Delta\gamma) + 2\beta\cos(\delta)}\right)d\delta \tag{37}$$

A numerical integration study indicates that

$$f(\beta, \Delta\gamma) = \begin{cases} -1 & if\ \beta > 1 \\ 0 & if\ \beta = 1 \\ 1 & if\ \beta < 1 \end{cases} \tag{38}$$

Substituting this result into (36) gives

$$\langle\Phi\rangle = \begin{cases} (\omega + \omega_{d,1})\Delta t & if\ \beta > 1 \\ \left(\omega + \frac{\omega_{d,0} + \omega_{d,1}}{2}\right)\Delta t & if\ \beta = 1 \\ (\omega + \omega_{d,0})\Delta t & if\ \beta < 1 \end{cases} \tag{39}$$

Removing the baseband frequency by substituting (13) into (39), we find that the period averaged Doppler estimated from the accumulated discriminator output is

$$\langle\widetilde{\omega}_d\rangle = \begin{cases} \omega_{d,1}, & if\ \beta > 1 \\ \frac{1}{2}(\omega_{d,0} + \omega_{d,1}) & if\ \beta = 1 \\ \omega_{d,0} & if\ \beta < 1 \end{cases} \tag{40}$$

In other words, the period-averaged Doppler estimate will track the Doppler of the NLOS component when the power of the NLOS component is larger ($\beta > 1$) and the LOS component when the power of the LOS component is larger ($\beta < 1$). The intermediate case is a special limiting case, where the step function (39) is singular, and where thus the value is approximated as the average of the function values on either side of the singularity. Practically speaking, a real system will only cross through

this singularity for a brief instant if the amplitude ratio β is changing, so for all intents the period-averaged Doppler frequency can be said to track the stronger signal component.

Note that our numerical approach to evaluating $f(\beta, \Delta\gamma)$ was to compute its value over a range of discrete β from 10^{-4} to 10^{4} on a log scale and over a range of discrete $\Delta\gamma$ from infinitely small ($\sim 10^{-6}$) to its theoretical limit $\pi/2$. Over 3000 cases were computed, and all agreed with (39) to numerical precision. In all case, the dummy variable δ was integrated from 0 to 2π. The final integral results are shown in Fig. 4.

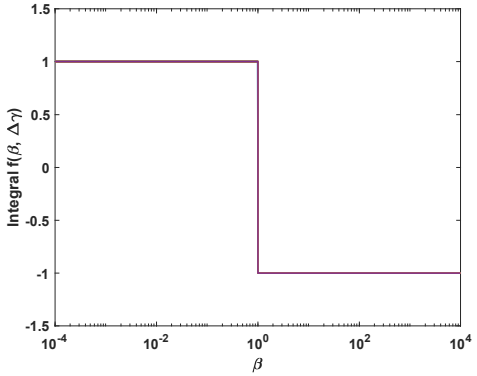

Fig. 4. Integral $f(\beta, \Delta\gamma)$ for all $\beta, \Delta\gamma$ considered

The plot shows a clear step function with respect to β. Interestingly, there is no variation in $f(\beta, \Delta\gamma)$ for changes in $\Delta\gamma$. The curves for different $\Delta\gamma$ are superposed in the figure, but no distinction is evident since all of the cases produce precisely the same curve.

PERIODIC VARIATION IN THE FLL OBSERVABLE FOR THE MULTIPATH CASE

In the case when a receiver is moving at a constant speed and experiences multipath, the FLL-derived Doppler observable varies periodically in time. This outcome contrasts with other cases considered (e.g. LOS only, NLOS only, and zero-speed cases), where the Doppler observable is simply proportional to speed. The question remains as to when multipath-induces oscillations are important and when the period-averaged result of Remark 3 is sufficient to model moving-receiver multipath. To answer this question, let us return to the model of the arctangent discriminator, as characterized by (35).

For a receiver moving at a constant velocity, the variable, periodic oscillations in the arctangent discriminator output are driven by a cosine term containing the variable δ, which is the only time-dependent variable in (35). The variable δ is a linear function of time *t*, as characterized by (33), so the value of the cosine term is periodic. By substituting (33) into (35), the frequency of the oscillation can be seen to be the beat frequency ω_{beat}, which is the difference of the frequencies on the two raypaths

$$\omega_{beat} = |\omega_{d,0} - \omega_{d,1}| \tag{41}$$

These periodic variations result in oscillations of the accumulated discriminator variable Φ. As consistent with the prior section and the rest of the paper, we continue to analyze NCO accumulation as occurring before filtering (rather than afterward, as shown in Fig. 3) because both filtering and accumulation are linear process, meaning equivalent outcomes are generated when the order of the processes are switched.

The amplitude ratio β factors strongly influences the periodic behavior of the accumulated discriminator Φ. To see this, it is useful to plot the accumulated discriminator Φ over a single period $T_{beat} = 2\pi/\omega_{beat}$, as is shown in Fig. 5 and Fig. 6. More specifically, the figures normalize Φ by Δt, to give the signal frequency with units (rad/s). The figures show a simulated case with the LOS component's Doppler shift equal to 302.5 rad/s and the Doppler shift of the NLOS component equal to 297.5 rad/s. The baseband frequency ω is arbitrarily set to zero in this example.

When the NLOS signal power dominates (β>1), the normalized discriminator $\frac{\Phi}{\Delta t}$ is clearly centered on the NLOS signal frequency, as shown on the left side of Fig. 5. The dashed line shows the extreme case ($\beta \to \infty$), where the normalized discriminator is a constant equal to $\omega_{d,1} = 297.5$ rad/s, as consistent with Remark 1. As β falls, a sinusoid-like ripple appears, which is clearly visible by the time $\beta = 10$. As the power continues to drop, the median value of the transient shifts upward

(toward the average frequency, $\frac{1}{2}\left(\omega_{d,0}+\omega_{d,1}\right)=300$ rad/s, but a sharp downward spike emerges in the middle of the period. This downward spike is responsible for balancing the period-averaged value of $\frac{\Phi}{\Delta t}$, so that it has a constant value of $\omega_{d,1}$ for all β>1, as described in Remark 3. A mirror image of this case is observed for the case when the LOS signal power dominates (β<1), as shown on the right side of Fig. 5. The difference is that when the LOS signal power dominates, the normalized discriminator output is centered on the LOS Doppler frequency $\omega_{d,0}=302.5$ rad/s, and with an upward spike rather than a downward one.

The intermediate case at β=1 is particularly interesting, because a singularity occurs here. The median value of the normalized discriminator is constant at the average value, 300 rad/s in this case, throughout the entire period except for one instant. At this instant, the denominator of (35) goes to zero, and so the output is undefined. Approaching from above (β>1), the spike appears to become a negative impulse function at the singularity, as shown in Fig. 6. Approaching from below (β<1), the spike appears to become a positive impulse function. This result is consistent with the step observed in the period-averaged value of the accumulated discriminator, as shown in Fig. 4.

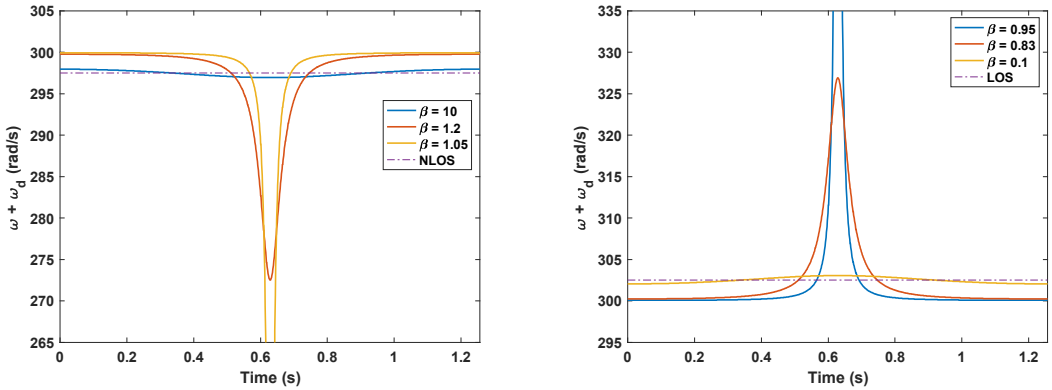

Fig. 5. Accumulated discriminator $\Phi/\Delta t$ over one period when $\beta>1$ (left) and $\beta<1$ (right)

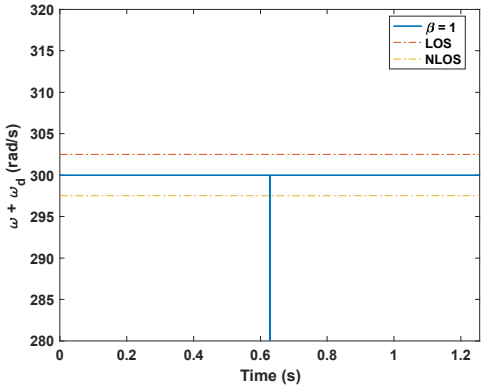

Fig. 6. Accumulated discriminator $\Phi/\Delta t$ over one period when $\beta\rightarrow 1$ from above

What remains is to consider the effect of filtering on the accumulated discriminator Φ, in order to interpret the effect of these oscillations on the FLL-derived Doppler output. The filtering process smooths sharp spikes in Φ, decreasing their magnitude and extending their duration. If the filtering process can sufficiently blur the spikes, the FLL-derived discriminator will essentially be a constant value (for constant receiver velocity), well modeled by the period-averaged result of (39). If the beat frequency is sufficiently slow, however, the loop filter output will be pulsatile, as the filter will track the periodic variations in Φ.

Analyzing filter effects is simplest in the limit when β is far from one. In these cases, the ripples in the discriminator output are small, and so the period-averaged model is accurate. As an example, consider the left side of Fig. 5, which shows the case for a high amplitude ratio ($\beta=10$), the ripple is small enough compared to the expected output that the period-averaged result (dashed line) is a very good approximation, regardless of the beat frequency.

Analyzing filter effects is more challenging when β approaches 1, as the amplitude of the perturbations in Φ begins to spike. To model this case, we will bound the perturbations as a chain of Dirac delta functions (impulses), occurring once per each beat period. We will call this series of delta functions a *spike chain*. The response of the filter to the spike chain is an accurate model for the case of $\beta = 1$, and an upper bound on perturbations for other values of amplitude ratio β (since amplitude decreases and extent increases for the spike as β moves away from one).

In modeling each spike in the spike chain, we can identify the amplitude as the area difference between the NLOS case (e.g. the dashed line in Fig. 5.) and the median of the $\beta \to 1$ case (e.g. the median of Fig. 6). The area difference of $\Phi/\Delta t$ is half the beat frequency times the beat period, which is π. Thus we can say that the amplitude of the impulse function is $\pm\pi$ rad/sec. The sign is negative when the dominant frequency is lower than the average frequency and positive when the dominant frequency is higher than the average frequency. For constant-velocity driving, the spike chain is a series of unit delta functions scaled by a magnitude of π, with $\frac{\Phi}{\Delta t} = \pm\sum_k \delta(t + kT_b)\pi$.

The filter output can be computed as the convolution of the filter impulse function $h(t)$ with the spike chain. If the filter time constant is longer than the beat period ($\tau > T_b$), then the filter output will be relatively flat, very close in value to the discriminator period average. However, if the filter time constant is shorter than the beat period ($\tau < T_b$), then the output of the loop filter will track the spike chain. In other words, in the $\tau < T_b$ case, the output of the filter will spike sharply and then decay back to a baseline value of $\omega_{av} = \frac{\omega_{d,0}+\omega_{d,1}}{2}$.

To proceed further, let us assume a representative model for the combined filtering that converts the discriminator output into the FLL-derived observable. Specifically, let's model the filtering process as a first-order filter with a bandwidth of 1 Hz. This filter has a time constant of $\tau = \frac{1}{2\pi}$ s. Convolving this filter's impulse function with the spike chain, we obtain the result that each spike increases the filter output by $\Delta\tilde{\omega} = 2\pi^2$ 1/s. We can convert this frequency jump to an equivalent speed jump using (16). This is to say that an impulsive bump in frequency by $2\pi^2$ 1/s is equivalent to a bump in estimated projected speed by $\Delta v = 0.60$ m/s. The initial perturbation decays away, but new perturbations are added each beat period. The result is that several of these decayed bumps can accumulate to produce a net perturbation over time. Once the system converges to a periodic steady state, the net perturbation might be described in terms of its minimum and maximum values.

Minimum and maximum perturbations are illustrated in Fig. 7, both in an absolute sense (top) and in a relative sense (bottom). The absolute plot shows perturbations in velocity units (m/s) as a function of beat period T_b. In the plot, the top of the shaded region shows the maximum value of the perturbation over each period, and the bottom of the shaded region shows the minimum. Values on the vertical axis are referenced to the period-averaged result, with positive perturbations Δv shifted toward the average Doppler and negative perturbations shifted away from the averaged Doppler. The difference between the top and bottom is always equal to the step change injected by a single impulse ($\Delta v = 0.60$ m/s), regardless of beat period. The deviation from the period-averaged reference does shift with beat period, however, progressing from symmetric variations about the reference (on the left side of the plot, where the beat period is short and smoothing is effective) to one-sided variations (on the right side of the plot, where the beat period is long and smoothing is ineffective).

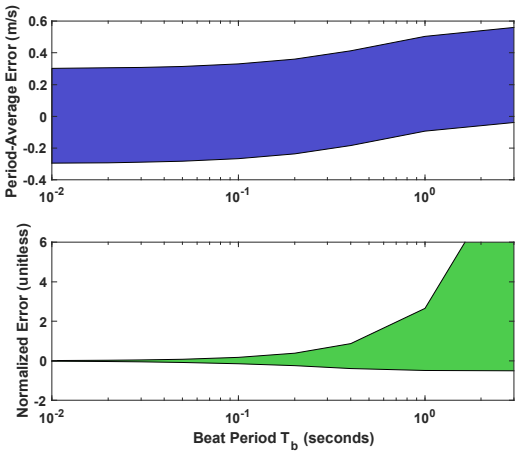

Fig. 7. Bounds on period steady-state errors for loop filter (top) in absolute terms with units of m/s and (bottom) in normalized terms, unitless

Although the absolute magnitude of the perturbations is always the same, as shown on the top of Fig. 7, the relative magnitude of these perturbations as compared to the difference between LOS and NLOS outputs is a strong function of the beat period. To study the relative effects, we normalize the perturbation in the FLL-observable by the speed difference between the LOS-only and NLOS-only results. Normalized perturbations are plotted as a function of beat period T_b on the bottom of Fig. 7. The normalization term (difference between outcomes for LOS and NLOS-only cases) is inversely proportional to T_b. As such, the normalization is very large when T_b is small, which means that the perturbations are very small compared to the NLOS errors in the short T_b case (when smoothing is effective). The size of the perturbations is very large compared to the normalization, however, for large T_b (when smoothing is not effective).

EXPERIMENTAL COMPARISON

In order to ground our theoretical results, we implemented an experimental data collection effort using a low-cost GPS receiver placed in a high-multipath environment. Specifically, we collected data for a pair of SiRF GlobalSat BU-353 USB GPS receivers set up as a differential reference station and a mobile receiver. Although we do not know the specific design characteristics that determine how the Doppler observable is computed by this chipset, we conjecture that many of our key results (specifically, Remark 1 through Remark 3) are largely independent of system implementation.

For the experiments, the reference station was placed in the center of a stadium, with a good view of the sky, such that the reference receiver would always track the LOS signal. The mobile receiver (or *rover*) was mounted onto a car. The rover was tested in three scenarios: 1) motionless in an open sky environment; 2) motionless in an urban canyon; and 3) driving in urban canyon. The three test scenarios were designed to establish the nominal noise levels for the differential Doppler measurements and, thereby, to allow comparison between open sky and urban canyon cases for a motionless rover (scenarios 1 and 2) or between stationary and moving cases in the high-multipath environment (scenarios 2 and 3).

The multipath errors on the pseudorange and Doppler measurements of the mobile receiver can be modeled as

$$\epsilon_\rho = \rho - \|\boldsymbol{p}_t - \boldsymbol{p}_r\| \tag{42}$$

$$\epsilon_\omega = \frac{\lambda}{2\pi}(\widetilde{\omega}_d - \widetilde{\omega}_t) + \tilde{\mathbf{v}}_\mathbf{r} \cdot \hat{\mathbf{u}}_{r,LOS} \tag{43}$$

where the position truth of the rover station is known from the map labelling and denoted as $\boldsymbol{p}_r = (x_\mathrm{r}, y_\mathrm{r}, z_\mathrm{r})$. The position of one satellite is $\boldsymbol{p}_t = (x_t, y_t, z_t)$, which is obtained from the downloaded precise ephemeris. The unit pointing vector was assumed to be aligned with the direction from the receiver to the satellite is $\hat{\mathbf{u}}_{r,LOS} = \frac{\boldsymbol{p}_t - \boldsymbol{p}_r}{\|\boldsymbol{p}_t - \boldsymbol{p}_r\|}$. The LOS subscript has been added to signify that this is an assumed pointing vector (and that the assumption may be incorrect in the event of multipath). The velocity $\tilde{\mathbf{v}}_\mathbf{r}$ describes the speed of the car, which is equal to velocity of the mobile receiver for straight-line driving. Note that car speed was obtained by manual processing of video of the vehicle's odometer reading. (In recent work, we have begun to automate speed measurement using an OBD reader [12].)

The pseudorange and Doppler measurements were differentially corrected subtracting the stationary-receiver observables from the rover observables at each epoch. If we appeal to the period-averaged model, we expect the Doppler observable will track only one signal (either the LOS signal or an NLOS signal) on average, but we do not which signal. As such we expect the differential Doppler will estimate the projected velocity for the mobile receiver $\widetilde{\omega}_t$ subject to a small bias due to the difference in projected satellite velocity. This small bias $\delta\widetilde{\omega}_t$, which can be removed in post-processing, is described as follows, where the the leading superscripts *mo* and *st* refer to the mobile and stationary reference receivers respectively:

$$\frac{\lambda}{2\pi}\delta\widetilde{\omega}_t = \mathbf{v}_t \cdot \left({}^{mo}\hat{\mathbf{u}}_{r,LOS} - {}^{st}\hat{\mathbf{u}}_{r,LOS}\right) \tag{44}$$

The satellite instantaneous satellite velocity is $\mathbf{v}_t$. Since the mobile and reference receivers are nearby (within less than 1 km), this correction term is relatively small, with a magnitude less than 0.03 m/s in our experiments.

In our postprocessing, we also took care to remove receiver clock trends. The slow clock drift that occurred over 80 seconds of data collection was estimated using the built-in Matlab function `smoothdata` and subtracted from the data, effectively removing the low-frequency content of the differential corrected observables. In the Doppler measurements we also observed high-frequency dithering at half the sample rate, with the computed signal jumping up and down at alternating time steps,

presumably due to a discretization internal to the receiver. To remove this high-frequency dithering, we applied a two-point sliding average.

Stationary Receiver in Open Sky and Urban Canyon Environments

This section presents a comparison of data for the two stationary experimental scenarios, one with the mobile receiver in open sky and the other with the mobile receiver in the urban canyon. Remark 2 predicts that the differential Doppler due to the mobile-receiver's motion $\delta\tilde{\omega}_r$ will be an unbiased estimate, that is $\delta\tilde{\omega}_r = 0$. Remark 2 does not make a prediction about the relative level of the background noise between the two cases, but we expect that the measurement noise will be higher in the urban canyon scenario, if only because the carrier-to-noise ratio C/N_0 is reduced for some satellites due to the presence of tall nearby structures.

Indeed, the data indicate that the differential Doppler measurement of receiver motion $\delta\tilde{\omega}_r$ appears unbiased, which is equivalent to the error $\delta\epsilon_\omega$ having zero mean. We show this for a representative example in Fig. 8, which plots the error $\delta\epsilon_\omega$ for satellite PRN 3 in the open sky case (left) and multipath case (right). For comparison, the differential pseudorange error is also plotted (top row) next to the differential Doppler (bottom row). Note that $\delta\epsilon_\omega$ was computed by differencing (43) between receivers, and $\delta\epsilon_\rho$ by differencing (42) across receivers.

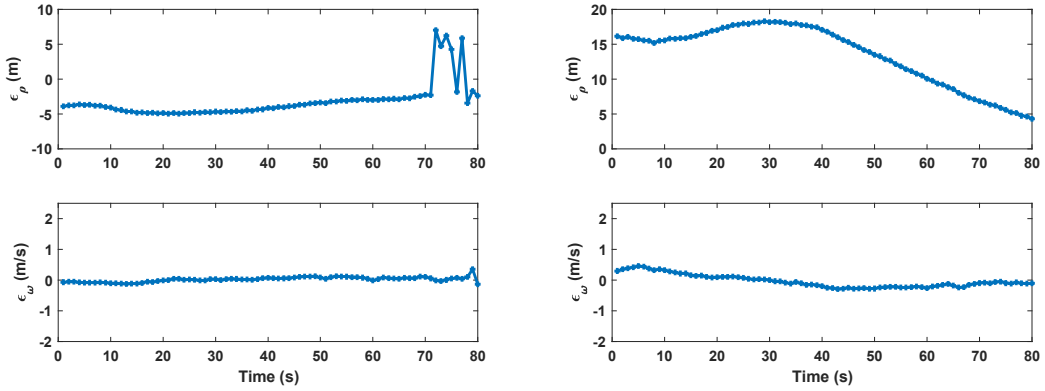

Fig. 8. Measurement errors for static receiver in open sky (left) and urban canyon (right)

This plot shows that the pseudorange plots are strongly affected by multipath, while the Doppler for the stationary receiver is relatively unaffected. The most reasonable explanation for the large variations in the differential pseudorange is multipath. It should be noted that the description "open sky" is used loosely for the mobile receiver, which was located 50 m from a four-story building in the case shown on the left; some multipath is seen in this case (left top), but only in the last 10 seconds, as evidenced by the step change in differential pseudorange error seen shortly after second 70. Pseudorange errors are even larger and more persistent in the urban-canyon data (right top), where pseudorange errors vary slowly over the 80 second window. By comparison, the Doppler errors are nearly flat in both the open sky and urban canyon cases, with errors under 0.5 m/s.

Stationary and Moving Rover in Urban Canyon

This section presents a comparison of data for the two urban-canyon scenarios, one with the mobile receiver stationary and the other with the mobile receiver moving. In the moving case, the car traveled in a straight line, accelerating at a roughly constant rate from 0 m/s to 3.5 m/s and then decelerating back to 0 m/s over a period of slightly less than 20 s. The vehicle speed profile, sampled at 1 Hz, is plotted in Fig. 9. It is convenient to subdivide this rover-moving case into three periods, as differentiated by two red dashed lines in Fig. 14. The middle period, between the two lines, is the period when the rover is moving.

Pseudorange and Doppler errors are again considered as a function of time for PRN 3, as plotted in Fig. 10. The pseudorange error plot (top) clearly indicates multipath. While driving, the pseudorange error increases from approximately zero to a distinctly non-zero value; this transition happens approximately when the vehicle starts moving (first red line) and grows progressively worse over time, presumably because the LOS signal power grew progressively weaker as compared to the NLOS signal power while the rover was moving.

The impact of the multipath on the Doppler error is different. The Doppler error (Fig. 10, bottom) tracks the car's speed profile (Fig. 9). In the absence of multipath, the car's speed is subtracted from the Doppler error when computing (43); in this case,

some residual Doppler error remains, which is proportional to the car's speed profile (reaching a peak Doppler error of approximately 1.5 m/s, as compared to the peak speed of 3.5 m/s). Evidently, the differential Doppler is proportional to but not equal to the car's speed.

The residual Doppler error can be explained by Remark 1. Remark 1 suggests that if the Doppler-observable is based on tracking an NLOS signal (only) then the measured receiver-motion component of Doppler will be scaled by the cosine of the NLOS angle-of-arrival $\theta_{r,NLOS}$. Because we assume the LOS angle-of-arrival $\theta_{r,LOS}$ in compute the differential Doppler error via (43), a residual difference remains: $\frac{\lambda}{2\pi}\delta\tilde{\omega}_r = \|\mathbf{v}_r\|\left(\cos\left(\theta_{r,NLOS}\right) - \cos\left(\theta_{r,LOS}\right)\right)$. This residual Doppler error is expected to be proportional to the vehicle speed, as observed for PRN 3 in Fig. 10 (bottom).

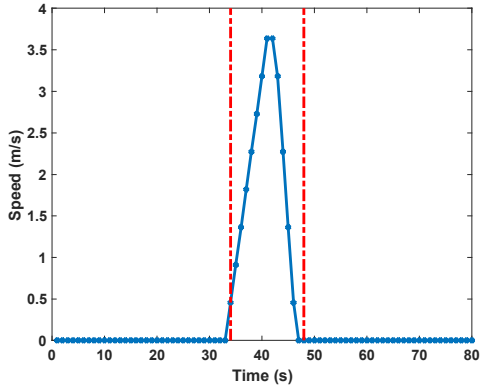

Fig. 9. Reference vehicle speed in dynamic test

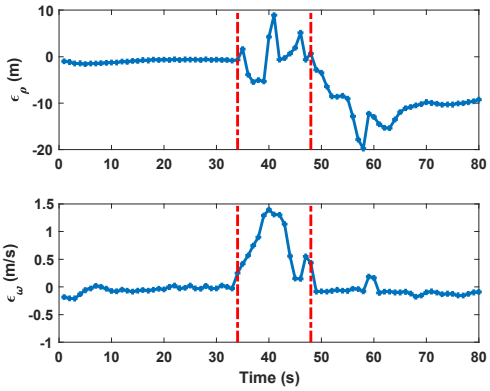

Fig. 10. Measurement error for dynamic receiver in multipath environment

In order to develop stronger support for Remark 1, it is useful to consider other satellites observed during the same trial. Because the speed-correction partially masks the NLOS error, let us consider the direct estimation of $\delta\tilde{\omega}_r$, the receiver-contribution to Doppler. The direct estimate $\delta\tilde{\omega}_r$ is equal to the error ϵ_ω without applying the nominal velocity correction ($-\tilde{\mathbf{v}}_\mathbf{r} \cdot \hat{\mathbf{u}}_{r,LOS}$). The direct estimates of $\delta\tilde{\omega}_r$ are shown for four satellites (PRN 14, 3, 31, and 16) in Fig. 11. For each PRN, the nominal speed correction ($-\tilde{\mathbf{v}}_\mathbf{r} \cdot \hat{\mathbf{u}}_{r,LOS}$) is plotted as a red dashed.

As expected, the Doppler signal tracks the nominal correction for some satellites in the absence of multipath. Such a case is shown for PRN14, as seen in Fig. 11(a). This subplot shows the measurement and model nearly overlap.

Multipath effects are seen for other satellites, particularly those with low C/N_0 values. The case of PRN 3 is a good example, as seen in Fig. 11(b). In this case, measured $\delta\tilde{\omega}_r$ is proportional to the speed computed with the LOS model, but scaled incorrectly due to the difference in arrival angle for the NLOS signal. A similar result is seen for PRN 16, as shown in Fig. 11(b), except that the scale factor is negative. Negative scale factors are indicative of a case when the car is driving toward the reflector and away from the satellite (or vice versa).

It is relevant to note that the PRN 3 and PRN 16 cases might be pure NLOS signals (as described by Remark 1), but that they might also be cases when an NLOS signal simply dominates over the LOS signal (as described by Remark 3). Since Remark 3 indicates that, for a pair of arriving signals, the Doppler observable is expected to be dominated by the stronger of the two signals, the two remarks cannot be distinguished for the analysis of cases like PRN 3 and PRN16. In order to distinguish between the two remarks, we would need to find a special case in which the power of the received LOS signal fell during receiver movement, eventually transitioning from being greater than the received NLOS power to being less.

A possible transition case is shown in Fig. 11(c). This case appears to show a Doppler observable that tracks the reference curve well initially, to about 37 seconds into the data collection. At this point, the Doppler observable transitions quickly downward, possibly tracking an NLOS signal arriving opposite the LOS signal (i.e. tracking a reflected triangle with a negative sign). Although we cannot prove that this case represents a switch between tracking the LOS and NLOS signal, it is a possible explanation as justified by Remark 3.

One possible limitation of our hypothesis is that the transition in Fig. 11(c) is not immediate, occurring over times between 37 and 45, rather than instantaneously as suggested by the period-averaged model (39). However, it is also relevant to note that the step-change is highly sensitive to the modeled singularity at $\beta = 1$, and that actually measurement noise might just as easily push the discriminator transient peak up or down when $\beta \rightarrow 1$, which suggests that noise might push the Discriminator to switch randomly back and forth between both sides of the step as the amplitude ration transitions through the region of $\beta \approx 1$. Random noise-driven transitions would smooth the step, resulting in a more graduate ramp transition between LOS and NLOS tracking. This is an effect that should be modeled more rigorously in the future.

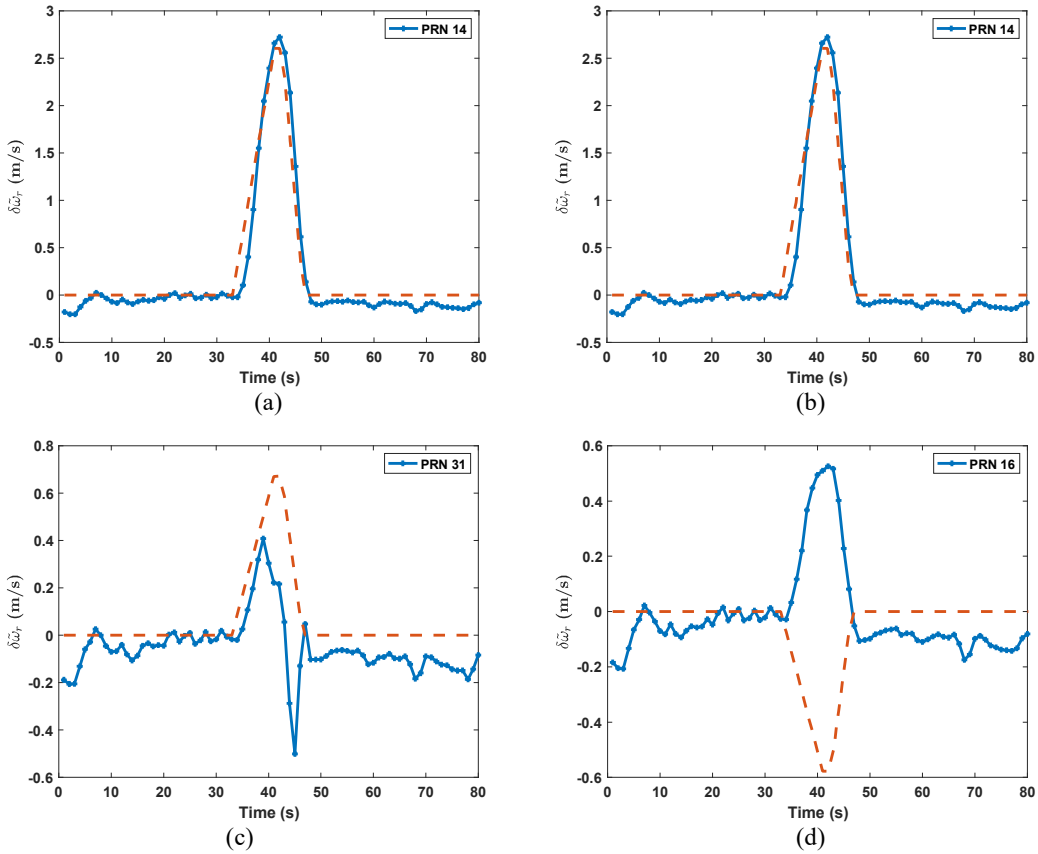

Fig. 11. Comparison between FLL-derived Receiver Doppler and the reference LOS projection for different satellites

NLOS DOPPLER AS A SIGNAL OF OPPORTUNITY

Under most circumstances, it is desirable to exclude Doppler measurements corrupted by NLOS signals, as discussed in [12]; however, in specific situations, NLOS and multipath signals may be useful as signals of opportunity. For an NLOS signal to be

useful as a signal of opportunity, its direction of arrival must be known. In concept, such directional information might be obtained, for example, from a beam-steering antenna.

Although beam-steering antennae are not common for civilian GPS applications, it is likely that cellular communication towers and users will equip beam-steering antennae (also known as multi-input multi-output or MIMO antennae) in the foreseeable 5G era [13]. Envisioning MIMO antennae as standard equipment and more multipath signals available due to emerging small-cell architectures, this section proposes an algorithm that would use both LOS and NLOS cell phone signals for velocity estimation. This concept of exploiting NLOS Doppler to improve velocity estimation has promise to complement other research on signal-of-opportunity navigation [14-17], which has focused primarily on position estimation rather than velocity estimation.

Our concept for velocity estimation from received Doppler signals is quite similar to velocity estimation in GPS, for which the measurement equation in [9] can be written:

$$\lambda f_d = \hat{\mathbf{u}}_l^{\mathrm{T}}(\mathbf{v} - \mathbf{v_t}) - \dot{b} \tag{45}$$

where λ is the communication wave length, f_d is the Doppler shift measurements in Hz and satisfies $f_d = \frac{\omega_d}{2\pi}$, $\hat{\mathbf{u}}_l^{\mathrm{T}}$ is the pointing vector to the l-th satellite, $\mathbf{v_t}$ is the velocity of the signal source (satellites in GPS), $\mathbf{v}$ is the receiver velocity, and $\dot{b}$ is the receiver clock drift. In contrast with a conventional GPS solution, where the geometric matrix is obtained from the position solution, our approach uses the beam boresight direction to estimate the AOA of each incoming signal. Using such an approach, the LOS and NLOS signals from the same cellular tower could potentially be separated, which would enable the same ranging source to provide multiple independent measurements that would aid in velocity estimation. In fact, given a sufficiently rich set of reflected signals and a sufficiently precise estimate of AOA for each signal, it is theoretically possible to obtain a large number of reflections from a single cell tower (noting that only four measurements are needed to solve four the three unknown components of velocity and the clock drift).

The velocity of a static base station is always zero. As for the reflectors, they are mostly composed of the ground and the building surfaces, which can also be assumed as stationary sources. Therefore $\mathbf{v_t}$ is zero and (45) is simplified into

$$\lambda f_{d,l} = \hat{\mathbf{u}}_l^{\mathrm{T}}\mathbf{v} - \dot{b} \tag{46}$$

The receiver velocity, together with the receiver clock drift can be estimated when the number of received signals $m \geq 4$. If the receiver is constrained to move parallel to the ground, as in an automotive application, then $m = 3$ (or even $m = 2$, if a rough receiver velocity estimation can be made by ignoring the clock drift term).

The error characteristics of the proposed velocity estimation can be evaluated using small perturbation analysis. The core part of this analysis is the uncertainty of the AOA measurements which perturb the measured pointing vector $\hat{\mathbf{u}}_l$ away from the truth $\mathbf{u}_l$. The perturbation is $\delta\mathbf{u}_l^T$:

$$\hat{\mathbf{u}}_N^{\mathrm{T}} = \mathbf{u}_l^T + \delta\mathbf{u}_l^T \tag{47}$$

If the cellular tower positions are well surveyed, and if the position of the receiver can be determined separately, then the pointing vector for the LOS signal can be determined in the conventional fashion, as in GPS. This is to say that $\delta\mathbf{u}_l^T$ can be assumed negligible for the LOS signal, for which the benefit of beamforming is simply increased receive power (and increased certainty that the correct signal component is being tracked).

For Doppler signals of opportunity, however, the perturbation $\delta\mathbf{u}_l^T$ will be directly related to the beamsteering algorithm (e.g., assuming the beam is steered toward the source to maximize carrier-to-noise ratio). In that case the perturbation $\delta\mathbf{u}_l^T$ will be characterized by an angle error. Specifically, the relevant angle error is in the estimate of $\theta_{r,l}$, which describes the angle between the pointing and velocity vectors.

The beamsteering AOA effect will increase the measurement error for estimation. This relationship can be determined by linearizing (46). The linearization of the measurement equation (46) gives the following, where $\tilde{\mathbf{v}}$ is the velocity estimate and $\tilde{\dot{b}}$ is the clock drift estimate:

$$\lambda\left(f_{d,l} + \delta f_{d,l}\right) = (\mathbf{u}_l^T + \delta\mathbf{u}_l^T)(\tilde{\mathbf{v}} + \boldsymbol{\delta}\mathbf{v}) - (\tilde{\dot{b}} + \delta\dot{b}) \tag{48}$$

Making the assumption that the higher-order term is small and moving the pointing-vector error to the left-hand side of the equation gives

$$\lambda f_{d,l} + \left(\lambda \delta f_{d,l} - \delta \mathbf{u}_l^T \tilde{\mathbf{v}}\right) \approx \mathbf{u}_l^T (\tilde{\mathbf{v}} + \delta \mathbf{v}) - \tilde{\dot{b}} - \delta \dot{b} \tag{49}$$

In this equation, the terms on the left in parentheses are the unknown measurement errors, and the $\delta \mathbf{v}$ and $\delta \dot{b}$ terms on the right are the unknown state-estimation errors. The state estimate can be obtained by stacking the measurement equations in matrix form. In creating this matrix, it is convenient to compile all of the measured unit pointing vectors $\hat{\mathbf{u}}_l^{\mathrm{T}}$ into the geometry matrix, augmenting each by a -1 to represent the scale factor for the clock drift. The result is an augmented geometry matrix **H**:

$$\mathbf{H} = \begin{bmatrix} \hat{\mathbf{u}}_0^{\mathrm{T}} & -1 \\ \hat{\mathbf{u}}_1^{\mathrm{T}} & -1 \\ \cdots & \\ \hat{\mathbf{u}}_N^{\mathrm{T}} & -1 \end{bmatrix} \tag{50}$$

The **H** matrix can be inverted in a least-squares sense (as the left pseudoinverse, denoted below by the trailing *L* superscript). Multiplying the pseudoinverse by the vector of Doppler measurements $\boldsymbol{f}_d$ gives the desired state estimate.

$$\begin{bmatrix} \tilde{\mathbf{v}} \\ \tilde{\dot{b}} \end{bmatrix} = \lambda \mathbf{H}^L \boldsymbol{f}_d \tag{51}$$

The state-estimation errors are related to the measurement-error vector $\delta \mathbf{m}$ by

$$\begin{bmatrix} \delta \tilde{\mathbf{v}} \\ \delta \tilde{\dot{b}} \end{bmatrix} = \mathbf{H}^L \delta \mathbf{m} \tag{52}$$

where the *l*-th entry of the measurement vector is

$$\delta m_l = \lambda\, \delta \boldsymbol{f}_{d,l} - \delta \mathbf{u}_l^T \tilde{\mathbf{v}} \tag{53}$$

The perturbation $\delta \mathbf{u}_l^T \tilde{\mathbf{v}}$ is the first-order term in an expansion of the dot product, or equivalently, the first-order term in the expansion of a cosine.

$$\delta \mathbf{u}_l^T \tilde{\mathbf{v}} = -||\tilde{\mathbf{v}}|| \sin\left(\theta_{r,l}\right) \delta\theta \tag{54}$$

The largest errors would occur when the nominal angle between the velocity and pointing vectors is 90°, in which case the sine term above becomes unity. To get a sense of the magnitude of the error for this worst-case, consider for instance, that the angular error is 1 degree and the vehicle speed is 30 mph (13.4 m/s). In that case, the error term $\delta \mathbf{u}_l^T \tilde{\mathbf{v}}$ could be as large as $1 \times \frac{\pi}{180} \times 13.4 = 0.23\, m/s$. Considering the Doppler measurement error is expected to be around $0.1\, m/s$ (in velocity units), we see that the beamsteering AOA effect is very similar in magnitude.

The advantage of the proposed method is that the Doppler shift measurements of all LOS and NLOS signals can be used for velocity estimation. This would turn the NLOS signals from a liability into an advantage. The resulting velocity estimates could be used directly, or they might be applied in other innovative solutions, such as integrity checking for the LOS ranging signals (which are significantly more vulnerable to multipath errors than Doppler signals) as described in [18].

FUTURE WORK

Many aspects of this work might be expanded in the future. One important detail is extending our FLL analysis to consider other design options, such as other discriminators, and to verify our analytic results with simulation. Also, we will seek to generalize our multipath results for two signals to the case of three or more signals. In cases of three or more signals arriving at the receiver, we hypothesize that only the FLL tracks only the signal with the highest amplitude, just as in the two-signal case; however, it remains to prove this result mathematically.

Additional future work relates to more fully developing the application outlined in Section V. For example, the performance of the proposed positioning algorithm should be fully evaluated, particularly with consideration given to the integrity requirements

of safety-critical applications like autonomous vehicle navigation. Also, additional work is required to evaluate actual beamforming strategies to determine how accurately the multipath signals can be separated in space.

CONCLUSION

This paper investigates the impact of NLOS and multipath signals on carrier-frequency tracking by the FLL. NLOS and multipath effects are analyzed theoretically, to model their effects on the Doppler observable. Our analysis leads to three key observations, based on an assumption that NLOS signals are reflected from stationary surfaces. First, in the case when only one NLOS signal component is tracked, the Doppler observable will be proportional to receiver speed, but the scale factor will be wrong. Second, in the case when a stationary receiver experiences multipath, the expected value of the Doppler observable will be correct, indicating the receiver speed is zero. Third, when a moving receiver experiences multipath, the FLL will tend to track the strongest received signal component (LOS or NLOS) as if the other signal components are absent. The last case has a caveat, which is to say that the moving receiver's FLL may experience additional time variations due to multipath, with those variations being periodic at a predictable beat frequency when the receiver speed is constant.

The three analytically-based observations were used to interpret experimentally acquired data. Though the details of the receiver hardware design were not known, the three analytically-based observations provided a reasonable interpretation of the data.

Based on the knowledge gained from the analyses and experiments, we proposed a novel approach to velocity estimation for a radio-navigation system featuring a beamsteering antenna. Such a system could combine AOA and Doppler shift measurements to distinguish LOS from NLOS signals. Moreover, the NLOS signals could be used as signals of opportunity to enhance velocity-estimation accuracy, since the only unknown needed to interpret NLOS Doppler is the arrival angle.

ACKNOWLEDGMENTS

The authors gratefully acknowledge the China Scholarship Council and the United States NSF (grant NSF 1836942) for financially supporting this research.

REFERENCES

[1] Cong, L. and Zhuang, W. "Nonline-of-sight error mitigation in mobile location." IEEE Transactions on Wireless Communications 4, no. 2 (2005): 560-573.

[2] Wylie, M. P., and Holtzman, J. "The non-line of sight problem in mobile location estimation." In Universal Personal Communications, 1996. Record., 1996 5th IEEE International Conference on Universal Personal Communications, vol. 2, pp. 827-831. IEEE, 1996.

[3] Le, B. L., Ahmed, K., and Tsuji, H. "Mobile location estimator with NLOS mitigation using Kalman filtering." In Wireless Communications and Networking, 2003. WCNC 2003. 2003 IEEE, vol. 3, pp. 1969-1973. IEEE, 2003.

[4] Groves, Paul D. "Shadow matching: A new GNSS positioning technique for urban canyons." *The journal of Navigation* 64, no. 3 (2011): 417-430.

[5] Wang, Lei, Paul D. Groves, and Marek K. Ziebart. "GNSS shadow matching: Improving urban positioning accuracy using a 3D city model with optimized visibility scoring scheme." Navigation: Journal of the Institute of Navigation 60, no. 3 (2013): 195-207.

[6] Nam, Y. H., Ng, B. L., Sayana, K., Li, Y., Zhang, J., Kim, Y., and Lee, J. "Full-dimension MIMO (FD-MIMO) for next generation cellular technology." IEEE Communications Magazine 51, no. 6 (2013): 172-179.

[7] Fleury, B. H., Tschudin, M., Heddergott, R., Dahlhaus, D., and Pedersen, K. I. "Channel parameter estimation in mobile radio environments using the SAGE algorithm." IEEE Journal on selected areas in communications 17, no. 3 (1999): 434-450.

[8] Thomä, R. S., Landmann, M., and Richter, A. "RIMAX-A maximum likelihood framework for parameter estimation in multidimensional channel sounding." In Proceedings of the International Symposium on Antennas and Propagation (ISAP 04), pp. 53-56. 2004.

[9] Misra, P. and Enge, P. "Global positioning system: Signals, measurements and performance second edition." Massachusetts: Ganga-Jamuna Press (2006).

[10] Kaplan, E. and Christopher H. "Understanding GPS: principles and applications." Artech house (2006).

[11] Gebre-Egziabher, D. and Gleason, S. "GNSS Applications and Methods." Artech House (2017): 257-279.

[12] Xu, L., and Rife, J., "NLOS and multipath detection using Doppler shift measurements," *Proceedings of the 32nd International Technical Meeting of the Satellite Division of The Institute of Navigation (ION GNSS+ 2019)*, Miami, Florida, September 2019.

[13] Wymeersch, H., Seco-Granados, G., Destino, G., Dardari, D., and Tufvesson, F. "5G mmWave Positioning for Vehicular Networks." IEEE Wireless Communications 24, no. 6 (2017): 80-86.

[14] Rabinowitz, Matthew, Spilker, James J., Jr., "Augmenting GPS with Television Signals for Reliable Indoor Positioning", *NAVIGATION, Journal of The Institute of Navigation*, Vol. 51, No. 4, Winter 2004-2005, pp. 269-282.

[15] Raquet, John F., Miller, Mikel M., Nguyen, Thao Q., "Issues and Approaches for Navigation Using Signals of Opportunity," *Proceedings of the 2007 National Technical Meeting of The Institute of Navigation*, San Diego, CA, January 2007, pp. 1073-1080.

[16] Khalife, Joe, Shamaei, Kimia, Kassas, Zak M., "A Software-Defined Receiver Architecture for Cellular CDMA-Based Navigation," *Proceedings of IEEE/ION PLANS 2016*, Savannah, GA, April 2016, pp. 816-826.

[17] Shamaei, Kimia, Kassas, Zaher M., "LTE receiver design and multipath analysis for navigation in urban environments", *NAVIGATION, Journal of The Institute of Navigation*, Vol. 65, No. 4, Winter 2018, pp. 655-675.

[18] Xu, L., and Rife, J., "Doppler-aided Line-of-sight Identification and Localization in Future Cellular Networks," *Proceedings of the 31st International Technical Meeting of the Satellite Division of The Institute of Navigation (ION GNSS+ 2018)*, Miami, Florida, September 2018, pp. 3018-3027.